

5-2014

Dust properties of $Z \sim 2$ infrared-luminous Lyman break galaxies.

Jennifer Leigh Wojno
University of Louisville

Follow this and additional works at: <https://ir.library.louisville.edu/etd>

 Part of the [Astrophysics and Astronomy Commons](#), and the [Physics Commons](#)

Recommended Citation

Wojno, Jennifer Leigh, "Dust properties of $Z \sim 2$ infrared-luminous Lyman break galaxies." (2014). *Electronic Theses and Dissertations*. Paper 1586.
<https://doi.org/10.18297/etd/1586>

This Master's Thesis is brought to you for free and open access by ThinkIR: The University of Louisville's Institutional Repository. It has been accepted for inclusion in Electronic Theses and Dissertations by an authorized administrator of ThinkIR: The University of Louisville's Institutional Repository. This title appears here courtesy of the author, who has retained all other copyrights. For more information, please contact thinkir@louisville.edu.

**DUST PROPERTIES OF $Z \sim 2$ INFRARED-LUMINOUS LYMAN
BREAK GALAXIES**

Jennifer Leigh Wojno
B.S., University of Louisville, 2012

A Thesis
Submitted to the Faculty of the
College of Arts and Sciences of the University of Louisville
in Partial Fulfillment of the Requirements
for the Degree of

Master of Science

Department of Physics and Astronomy
University of Louisville
Louisville, Kentucky

May 2014

DUST PROPERTIES OF $Z \sim 2$ INFRARED-LUMINOUS LYMAN BREAK GALAXIES

Jennifer Leigh Wojno
B.S., University of Louisville, 2012

A Thesis Approved on

April 15, 2014

by the following Thesis Committee:

Dr. Lutz Habertzettl

Dr. James T. Lauroesch

Dr. Gerard M. Williger

ACKNOWLEDGMENTS

I would like to extend my deepest thanks to my thesis advisor, Dr. Lutz Habertzettl, for providing me with invaluable guidance and advice throughout these past two years. The quality of his mentorship has helped me to grow not only as a student, but also as a professional astronomer. I would also like to thank my thesis committee members Dr. Gerard Williger and Dr. James Lauroesch for advising this work, and providing critical comments and suggestions. In addition, I would like to thank the Department of Physics and Astronomy at the University of Louisville for their financial support, especially Dr. Chakram Jayanthi for her support throughout my graduate career. I would also like to thank Matthew Nichols for his assistance with figuring out numerous bits of IDL code, and his contribution to this work (Figure 4). Finally, I would like to thank my fellow graduate students, my friends, and my family for their support and encouragement, especially Zach Colado for his patience and emotional support.

This work would have not been possible without the data provided by the GOODS-S, PEP, and HerMES survey teams, and I would like to thank them for making the data publicly available. This research has made use of data from HerMES project (<http://hermes.sussex.ac.uk/>). HerMES is a Herschel Key Programme utilising Guaranteed Time from the SPIRE instrument team, ESAC scientists and a mission scientist. The HerMES data was accessed through the Herschel Database in Marseille (HeDaM - <http://hedam.lam.fr>) operated by CeSAM and hosted by the Laboratoire d'Astrophysique de Marseille.

ABSTRACT

DUST PROPERTIES OF $Z \sim 2$ INFRARED-LUMINOUS LYMAN BREAK GALAXIES

Jennifer L. Wojno

April 15, 2014

Lyman break galaxies (LBGs) are well-known indicators of star formation. By analyzing the dust of moderate redshift ($z \sim 2$) LBGs, we can further investigate the properties of these strongly star forming galaxies at an epoch when global star formation is expected to peak. Using data observed by the *Herschel* satellite, we derive far-infrared fluxes for our color-selected sample of LBGs in the GOODS-S field, including a subsample of infrared-luminous LBGs (ILLBGs). This is one of the first samples of UV dropouts/partial dropouts, which are also infrared-luminous, to be studied for their far-IR properties. Fitting modified Planck curves and model spectral energy distributions (SEDs), we make estimations for dust temperatures and masses for our ILLBGs. We find dust temperatures ranging from $\sim 19 - 70$ K, with masses $\sim 5.2 \times 10^6$ to $3.3 \times 10^9 M_{\odot}$, and star formation rates on the order of $\sim 10 M_{\odot} \text{yr}^{-1}$.

TABLE OF CONTENTS

| | | |
|----------|---|-----------|
| 1 | INTRODUCTION | 1 |
| 2 | SCIENCE BACKGROUND | 3 |
| 2.1 | Galaxy Evolution | 3 |
| 2.2 | Lyman break Galaxies as Indicators of Star Formation | 5 |
| 2.3 | Dust in Star Forming Galaxies: Infrared-Luminous LBGs | 7 |
| 2.4 | Spectral Energy Distributions | 8 |
| 3 | DATA | 10 |
| 3.1 | GOODS-S Field | 10 |
| 3.2 | Selection Criteria | 11 |
| 3.3 | Instrumentation | 13 |
| 3.4 | Surveys | 15 |
| 3.5 | Herschel Interactive Processing Environment (HIPE) | 16 |
| 4 | ANALYSIS | 18 |
| 4.1 | Flux Measurements | 18 |
| 4.2 | SED Fitting: Planck Curves | 22 |
| 4.3 | SED Fitting: MAGPHYS | 24 |
| 5 | RESULTS AND DISCUSSION | 28 |
| 6 | SUMMARY AND CONCLUSIONS | 35 |
| | REFERENCES | 38 |
| | CURRICULUM VITAE | 40 |

LIST OF FIGURES

| | | |
|----|--|----|
| 1 | Madau plot (Madau & Dickinson 2014) | 4 |
| 2 | Lyman break at various redshifts | 6 |
| 3 | Spectral energy distribution for a sample LBG | 9 |
| 4 | Location of the GOODS-S field | 11 |
| 5 | Color-color diagrams used to obtain our LBG sample | 12 |
| 6 | Color-magnitude diagrams used to select ILLBGs | 12 |
| 7 | The <i>Herschel</i> Space Observatory | 14 |
| 8 | Postage stamp images | 20 |
| 9 | Postage stamp images | 21 |
| 10 | Modified blackbody fitting results | 23 |
| 11 | MAGPHYS fitting results | 26 |
| 12 | MAGPHYS fitting results | 27 |
| 13 | Luminosity correlation | 30 |
| 14 | Stellar mass vs star formation rate | 32 |
| 15 | Dust mass vs total mass for galaxy surveys | 34 |

1 INTRODUCTION

The study of galaxy evolution is a relatively old field, but has been re-ignited in recent years with advances in space-based telescopes and observational techniques. By studying various populations of galaxies at various redshifts, we aim to more accurately describe the formation and evolution of these galaxies, and how we arrive at galaxies such as our own Milky Way. Section 2 begins by highlighting the scientific background crucial for sufficient comprehension of this work. While it has been written with the assumption of a basic understanding of key concepts in physics, the realm of astrophysics includes many specific, technical details that may not be common knowledge. This scientific background also provides the motivation for this work; the study of galaxy evolution, and how furthering our understanding of the development and structure of galaxies over various wavelengths contributes to our understanding of the universe as a whole. The study of galaxy evolution aids us not only in understanding our cosmological history, but also provides us with a perspective on our future as inhabitants of the Milky Way. In this work, we focus on the rate of star formation in our sample of galaxies, as this is a key indicator to where they lie in the evolutionary scheme. In order to properly study this star formation rate, a number of factors must be considered. One of the key components in accurately measuring the star formation rate of a galaxy is measuring the amount of dust present in that galaxy, as dust may obscure light from young, bright stars.

Section 3 describes how our sample of galaxies were selected, and the data used to study this sample. It begins by describing the field in which our galaxy sample was selected, the GOODS-S field. We utilize observations of this field by space-based telescopes such as

Herschel and *Spitzer*, as the rate of star formation within these galaxies may be underestimated when using traditional ground based observations, due to dust obscuring some of the UV light from the galaxy (§ 2.2). As with any scientific endeavor, it is crucial for the characteristics of the instrumentation used to be adequately described, as the results and their possible limitations must be understood in the context of this instrumentation. Space telescopes are incredibly complex instruments, so only a brief description of their components is given. For more technical details, references can be found within these sections.

Section 4 provides an overview of the methods used to extract data from the observations, which are then used to explore the properties of our sample of galaxies. The theory of these applied methods, used in obtaining these results, are described in detail. An essential component of these analysis fitting our measured fluxes to model spectral energy distributions. In this work, we employ two distinct methods, each with its own benefits and shortcomings. In addition, we compare the results obtained using both methods, and comment on any variation in the measured characteristics. While the source code used in our analysis is not provided, it is available upon request.

In Section 5, we present the results of our analysis, including the results obtained in our SED fitting. These results are then compared to other results from the literature, and any distinctions are discussed. Finally, in § 6, we summarize our findings, examine how they compare to published results from similar works, and discuss the implications of our results. In addition, this section provides an final brief overview of the work done, highlighting the most important aspects of the research, and discuss how these results may be expanded through additional analysis, or new observations. Throughout this work, we assume a standard concordance cosmology of $H_0 = 71 \text{ km s}^{-1} \text{ Mpc}^{-1}$, $\Omega_M = 0.3$, and $\Omega_\Lambda = 0.7$.

2 SCIENCE BACKGROUND

2.1 Galaxy Evolution

Our understanding of galaxy evolution and growth has faced constant refinement over the past century, from Hubbles classification of galaxies (Hubble 1927) to current models, such as hierarchical clustering. While Hubble never intended his classification scheme to indicate a method of evolution (Baldry 2008), a relationship between elliptical and spiral galaxies was sought after by astronomers for much of the 20th century. In 1962, a top-down model of galaxy formation called monolithic collapse was proposed by Eggen, Lynden-Bell, & Sandage (1962), describing clouds of gas collapsing to form a galaxy all at once (Eggen et al. 1962). A decade later, the Toomres found evidence for a more hierarchical approach; mergers between two spiral galaxies result in the ellipticals we see in the local universe (Toomre & Toomre 1972). Today, hierarchical structures are a key component to the standard cold dark matter cosmological model (Λ CDM). This model offers additional refinement to evolutionary schemes, explaining how many of the morphological features of galaxies, such as disks, spheroids (or ellipticals), and bars, arise naturally through accretion and galaxy mergers (Steinmetz & Navarro 2002).

In order to construct more complete models of galaxy evolution, we must consider the star formation history of galaxies, as star formation relates directly to the color, size, and age of a galaxy. Throughout the past 20 years, significant advances have been made in moderate-to-high redshift astronomy, especially with respect to galaxy surveys. By finding and locating star forming galaxies at various redshifts, we can construct models of star formation throughout the universe, for any given point in time. The most recent sur-

veys suggest that the global star formation rate peaked around 10 billion years ago, which roughly corresponds to a redshift (or z) of 2 (e.g. Madau & Dickinson (2014)).

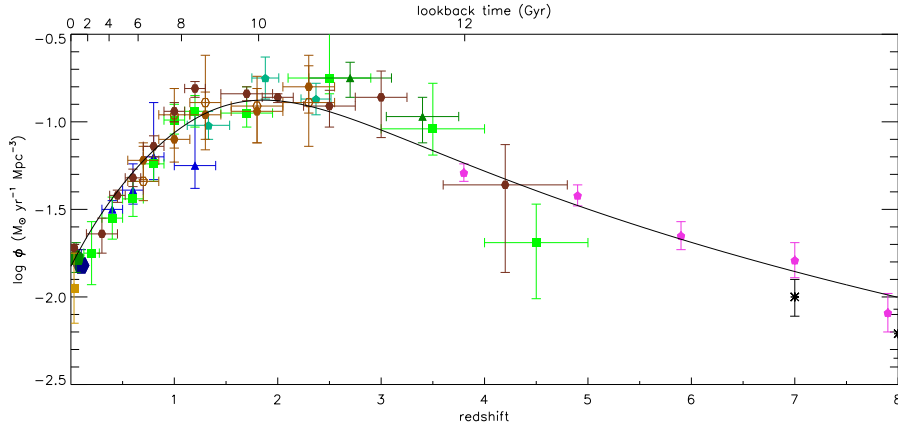


Figure 1: Star formation rate per Mpc^3 vs redshift, known as a Madau plot, adapted from Madau & Dickinson (2014). This plot illustrates the global star formation rate, peaking at approximately $z \sim 2$. Here, a number of results from approximately 13 surveys are shown, with redshift ranges $0.01 \leq z \leq 8.0$. Details on the data sets, as well as the line of best fit can be found in Madau & Dickinson (2014).

However, while star-forming galaxies in the higher redshift ($z \geq 3$) and local universe have been extensively studied, it has only recently become possible to properly study the redshift range of $z \sim 1 - 2$ through advances in space-based facilities. Galaxies in this so-called “redshift desert” are crucial for reconstructing the star formation history of the universe, as the peak of global star formation is expected in this range (Figure 1). Understanding the global star formation rate is crucial to understanding how galaxies develop and evolve; after all, galaxies are collections of stars. Through the observation of star-forming galaxies in this redshift range, a more sophisticated model for the development of these galaxies may be constructed.

2.2 Lyman break Galaxies as Indicators of Star Formation

For our study of star-forming galaxies at moderate redshift, we focus on Lyman break galaxies (LBGs). These galaxies provide good candidates for studies of populations of galaxies at moderate-to-high redshifts, as they are selected according to external properties (e.g. their Lyman break) rather than internal properties. By selecting galaxies in this way, we ensure a consistent sample over a range of redshifts. While young, hot stars emit primarily ultraviolet (UV) photons; anything shorter than 912\AA is usually absorbed by neutral gas surrounding the stars, as well as the intergalactic medium (IGM), creating a characteristic break in their spectra. Galaxies observed at higher redshifts will have their spectra, and therefore these identifying features, shifted to longer wavelengths as $912\text{\AA}(1+z)$ (Figure 2). For galaxies with $z \geq 3$, this Lyman break is shifted into the optical part of the spectrum, and has been well-studied through ground-based observations. However, for galaxies at $z \sim 1-2$, the Lyman break occurs around $\sim 1800-2100\text{\AA}$, which is in the observed-frame UV/NUV (see Figure 2). Therefore, space-based observations are necessary for galaxies at this redshift range, as a Lyman break would be difficult to discern due to absorption of UV photons by the Earth's upper atmosphere. A number of studies, such as Shapley et al. (2001), Reddy et al. (2008), Rigopoulou et al. (2006), and Magdis et al. (2010), have examined properties of LBG populations at $z \sim 3$. These studies show relatively massive LBGs, with estimated stellar masses of $5 \times 10^{10} M_{\odot} \sim 10^{11} M_{\odot}$ (Rigopoulou et al. 2006; Magdis et al. 2010), and star formation rates (SFR) in the order of 10's of solar masses per year (Shapley et al. 2001).

In order to detect these Lyman break galaxies at moderate redshifts, the UV dropout method (Steidel & Hamilton 1992) is used, as the Lyman break occurs in the observed-frame UV for our redshift range ($z \sim 1-2$). Broadband photometry is used to determine the flux of a galaxy through various filter bands around the expected position of the shifted Lyman break. Such objects will appear in the optical images, but not in the UV, which indicates a

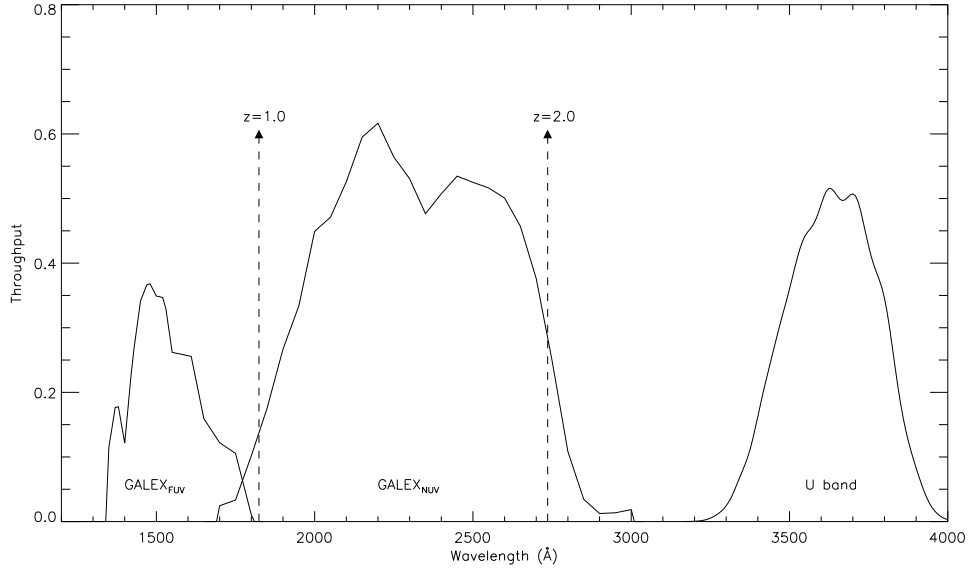


Figure 2: Lyman break at various redshifts. The dotted lines represent the position of the Lyman break shifted to the indicated wavelength. The filter bands used (GALEX NUV, GALEX FUV, and U band) are the filter bands used in determining the UV dropouts, which were selected for in our original LBG sample.

UV dropout. This method also provides a rough estimate of the redshift of the galaxy. As shown in Figure 2, the GALEX FUV (effective wavelength $\lambda = 1516 \text{ \AA}$)¹ and NUV ($\lambda = 2267 \text{ \AA}$) filters can be used to determine the position of the Lyman break for our galaxies. Prior to space-based observations, Lyman break galaxies were more commonly studied at epochs $z \geq 3$, as these galaxies will drop out further towards the observed-frame optical, where ground-based observations can be used, utilizing BM/BX and BzK selection methods (Adelberger et al. 2004; Steidel et al. 2004; Daddi et al. 2004). The BM/BX method as described in Steidel et al. (2004) selects for star-forming galaxy populations at certain redshifts ($z = 1.70 \pm 0.34$ and $z = 2.20 \pm 0.32$ for “BM” and “BX” galaxies, respectively), according to their colors in specific optical filters. The BzK selection method as described in Daddi et al. (2004) also employs a color selection criteria, utilizing the B , z , and K optical filters. While these methods can be used to select samples of star forming galaxies comparable to $z \leq 3$ LBGs while avoiding the issue of having to use space-based observations, in order to ensure consistent comparison, we want to correlate the properties of our

¹http://galexgi.gsfc.nasa.gov/docs/galex/Documents/ERO_data_description_2.htm

selection of galaxies to other comparably selected samples.

2.3 Dust in Star Forming Galaxies: Infrared-Luminous LBGs

In addition to absorption by neutral hydrogen, a portion of the UV light greater than 912\AA emitted from the star-forming regions in LBGs may be scattered by dust. For our purposes, dust is simply small grains composed of carbon and silicon, around a few microns in size. Studying dust in the early universe may aid in better understanding when this dust was formed, and how it affects the evolution of certain populations of galaxies. The existence of metals (i.e. elements heavier than hydrogen and helium) in the ISM is made possible through supernovae, which may indicate certain generations of star formation. For galaxies younger than $\sim 10^9$ years ($z \sim 5 - 6$), only Type II supernovae contribute to the total dust mass, due to the short lifespan of young, massive stars. (Takeuchi & Ishii 2004; Hirashita & Ferrara 2002). For galaxies older than 10^9 years, Type I supernovae and giant-branch stars (AGB/RGB) may also contribute to the total dust mass for star-forming galaxies. The formation and abundance of this dust is understood to have an effect on the star formation rate of the galaxy, as dust grains allow for efficient formation of molecular hydrogen (H_2), which in turn cools the gas in the ISM, increasing the rate of star formation.

While mid-infrared ($\sim 3-10\ \mu\text{m}$, $\sim 24-160\ \mu\text{m}$) observations of galaxies with instruments such as *Spitzer* can allow for the identification of more complex molecules associated with dust particles, such as polycyclic aromatic hydrocarbons (PAHs), we will focus on far-infrared (far-IR) thermal emission of dust, not molecular vibrations. These dusty galaxies become brighter in the infrared (IR), as UV light from young stars is absorbed by dust, and re-emitted in the far-infrared (far-IR). LBGs which are bright in the IR are called infrared-luminous LBGs (ILLBGs). Understanding the role of dust in our LBGs is crucial when estimating star formation rates, as the abundance of star formation is often underestimated

due to dust, which obscures regions of star formation. In addition, studying dust emission from LBGs and ILLBGs may aid in constructing a more accurate view of the cosmic infrared background (CIB), which is similar to the well-studied cosmic microwave background (CMB) at infrared wavelengths. In addition to local star-forming galaxies such as Luminous Infrared Galaxies (LIRGs), and Ultra Luminous Infrared Galaxies (ULIRGs), as well as high-redshift galaxies such as sub-millimeter galaxies (SMGs), star-forming galaxies such as LBGs may have a significant contribution ($\sim 20\%$) (Webb et al. 2003) to the CIB, which may further constrain models for global star formation rates.

From our original sample of 73 LBGs at $z \sim 1 - 2$, we have identified a small subsample of 14 ILLBGs, which may represent a significant portion of the overall star formation rates in galaxies at this redshift (Haberzettl et al. 2012). The properties of these galaxies make them analogous to sources in the local universe, such as LIRGs and ULIRGs (Petty et al. 2009). By comparing the physical characteristics of these galaxy populations, such as dust masses and temperatures, we can more accurately impose constraints on star formation processes at higher redshifts.

2.4 Spectral Energy Distributions

A spectral energy distribution (SED) is simply a measure of an object's flux over a certain wavelength range. An example model SED for one of the galaxies in our sample is shown in Figure 3. There are a number of features that denote distinct regimes due to emission from various sources within a galaxy. Wavelengths shorter than $\sim 8 \mu\text{m}$ are considered to be purely due to stellar contributions: spectral emission and absorption features from atomic excitations (e.g. H, N lines). For wavelengths from $\sim 8 - 50 \mu\text{m}$, the emission is due to a mix of complex molecules such as PAHs (Dale et al. 2001), as well as the contribution due to stellar emission. For wavelengths longer than $\sim 50 \mu\text{m}$, the emission

is considered purely thermal emission due to large, complex carbon and silicate grains of dust. As our sources are infrared-luminous, we expect that the peak of their emission due to re-absorption by dust to lie somewhere in the far-IR range ($\sim 50 - 1000 \mu\text{m}$). This thermal emission due to dust behaves approximately as a blackbody. That is, it can be considered a near-perfect absorber and emitter of incident radiation. A Planck curve can be used to model the SED of a blackbody (in this case, the dust in our galaxies) for a given temperature. From this model, certain parameters of the dust, and therefore information about star formation within the galaxy, can be determined. Details on the fitting procedures used to fit the SEDs for our sample of galaxies can be found in § 4.2 and § 4.3.

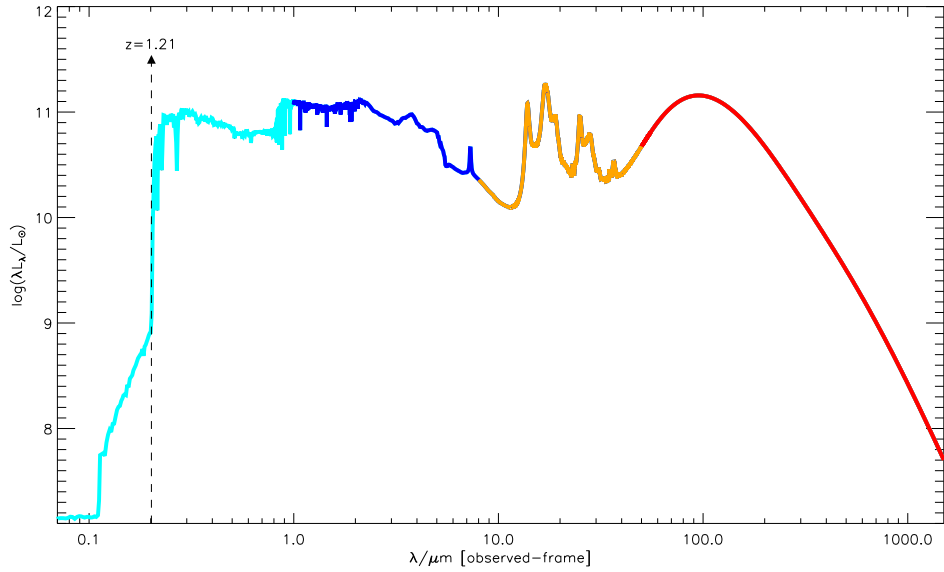


Figure 3: Example model SED for one of the galaxies in our sample. For this object, the Lyman break is very obvious, and fits with the object’s given photometric redshift. The emission at wavelengths shorter than $8 \mu\text{m}$ is considered a purely stellar emission (blue), where the cyan indicates the stellar contribution from young stars ($\leq 1 \mu\text{m}$), and the blue indicates the stellar contribution from the older stellar population ($\sim 1 \mu\text{m} \leq \lambda \leq 8 \mu\text{m}$). $8 \mu\text{m} \leq \lambda \leq 50 \mu\text{m}$ is considered a mix of dust and stellar emission (orange), and emission greater than $50 \mu\text{m}$ is considered purely due to dust (red). As described in § 2.4, we focus on the far-IR thermal emission due to dust, which dominates the wavelength range from $\sim 70-1000 \mu\text{m}$.

3 DATA

Our sample of 14 ILLBGs were color-magnitude selected using ground-based optical data and *Spitzer* data (Haberzettel et al. 2012). For this study, we used *Spitzer* 24 μm priors to verify the locations of the objects in our sample. To derive dust properties, we used publicly available far-IR data of the GOODS-S field which were observed by two instruments, PACS and SPIRE, on-board the *Herschel* Space Observatory. The observations by *Herschel* were publicly available via the PEP (PACS Evolutionary Probe)² and HerMES (Herschel Multi-tiered Extragalactic Survey)³ surveys for the PACS and SPIRE data, respectively. Table 1 summarizes the data relevant to survey coverage, instrumentation, and detector properties.

3.1 GOODS-S Field

The GOODS-S field is located within the Chandra Deep Field South (CDFSS), centered at 3h 32m 30s, $-27^{\circ}48\text{m }20\text{s}$, covering an area of 160 square arc minutes ($10'$ by $16'$). These deep fields are selected primarily for their low density of bright, close objects such as stars within our own Galaxy or other obscuring factors such as interstellar gas and dust. In this sense, these fields are essentially “blank”, and are well suited for studying faint, distant galaxies. The GOODS-S field is well-observed, with extensive coverage from both ground and space-based observatories, from X-rays to radio: GALEX with NUV/UV, Hubble Space Telescope with UV, optical, and near-IR, *Spitzer* with high resolution mid-IR observations, and *Herschel* with extensive far-IR coverage.

²<http://www.mpe.mpg.de/ir/Research/PEP/index.html>. Using combined *Herschel*-PACS data from the PEP (Lutz et al. 2011) and GOODS-*Herschel* (Elbaz et al. 2011) programs, as described in Magnelli et al. (2013).

³<http://hermes.sussex.ac.uk/>

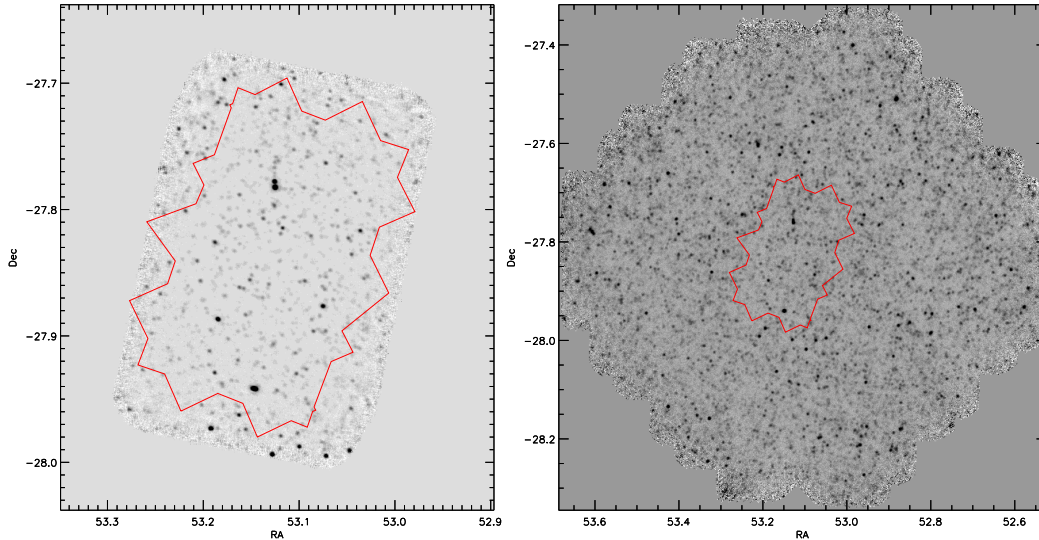


Figure 4: Location of the GOODS-S field. The left panel shows the location of the GOODS-S field overlaid on PACS (§ 3.3) 160 μm data, while the right panel shows the GOODS-S field overlaid on SPIRE (§ 3.3) 250 μm data. Image credit: Matthew Nichols.

3.2 Selection Criteria

LBG candidates were selected by cross-correlating SExtractor searches of the GOODS-S field in multiple filter bands, as described in Habertztl et al. (2012). These possible candidates were further identified as LBGs by utilizing color-color plots (Figure 5). Model galaxy color tracks were derived using HyperZ (Bolzonella et al. 2000) for a variety of physical properties such as age, and star formation rate, as well as dust properties. These model color tracks were then used to guide the definition of the limits for the $B - R$ vs $U - B$, and $U - B$ vs $NUV - U$ colors of each galaxy. These color cuts, along with general LBG sample, are shown in the left and right plots of Figure 5, respectively. This sample was then cleaned for stellar contamination, and limited to those objects identified in 10 of the 14 filter bands used, from the U to 4.5 μm filter bands (Habertztl et al. 2012). The final sample contained 73 LBG candidates, 53 of which were NUV-dropouts, and 20 were NUV-selected. In addition, the sample contains a subsample of 14 ILLBGs, which was obtained using color-magnitude diagrams to select for those galaxies which had very red colors, meaning that they are bright in the IR (Figure 6). For this work, we focus on our

subsample of 14 ILLBGs.

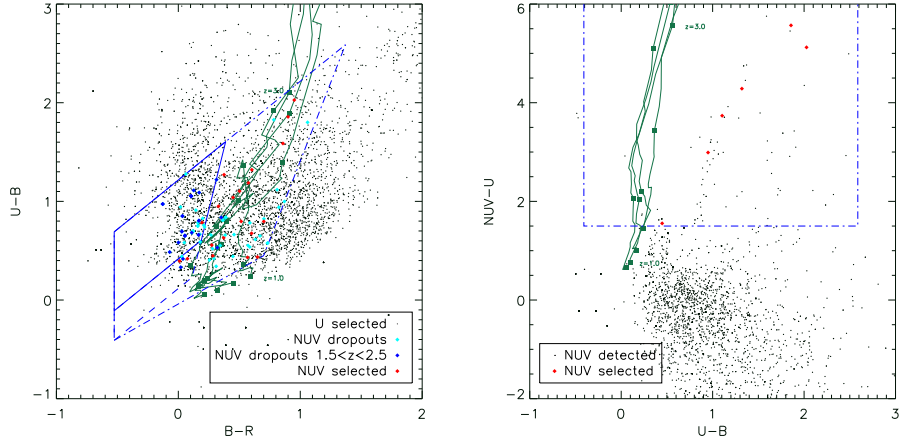


Figure 5: Color selection criteria employed to obtain our LBG sample. The symbols for the objects are explained in the legend. The dark green lines are the color tracks of 4 different model SEDs: burst 0.5 Gyr old, exponential decreasing SFR 0.5 Gyr old, exponential decreasing 1 Gyr old, and an irregular galaxy as defined in a HyperZ model SED (Bolzonella et al. 2000). The dark green squares mark the redshifts, from $z = 1.0$ to $z = 3.0$ in intervals of $dz = 0.5$. The blue boxes (solid, dashed, and dashed-dotted) are the same as described in Habertzettl et al. (2012).

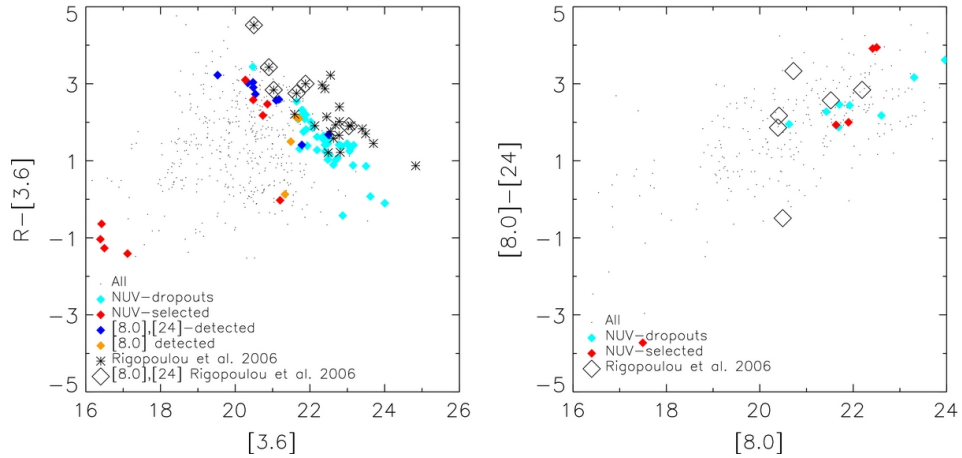


Figure 6: Color-magnitude diagrams used to select the ILLBG sample from the general LBG sample (Habertzettl et al. 2012). The $z \sim 3$ LBG sample (i.e., those galaxies with very red colors) described in Rigopoulou et al. (2006) was used as a comparison to determine LBGs from our sample which were infrared-luminous (ILLBGs). The final sample of 14 ILLBGs used in this work is shown on the right hand side.

3.3 Instrumentation

Observations of the GOODS-S field by two space-based telescopes were used for this work: the *Herschel* Space Observatory and the *Spitzer* Space Telescope. *Spitzer* provided data priors, used to verify the location of our objects, while *Herschel* provided data of the GOODS-S field used in our analysis. In addition, the Large Apex Bolometer Camera and Array (LABOCA) instrument on the ground-based Atacama Pathfinder Experiment (APEX) radio telescope provided upper limits for far-IR data via the LABOCA Extended Chandra Deep Field South (ECDFS) Submillimetre Survey (LESS) (Weiß et al. 2009).

The *Herschel* Space Observatory

Launched on May 14th, 2009, the *Herschel* Space Observatory (Figure 7) provided unprecedented coverage and resolution for crucial observations of the far-infrared and sub-millimeter universe (Pilbratt et al. 2010). *Herschel* observed both the local and high redshift universe, focusing in particular on dusty galaxies that would have otherwise been unobservable by ground-based telescopes due to absorption by the Earth’s atmosphere. Within our own Galaxy, *Herschel* aimed to study the relationship between star formation and the interstellar medium (ISM). In order to survey these long, low energy wavelengths, liquid helium was used to cool the telescope and the three scientific instruments on board: the Heterodyne Instrument for Far Infrared (HIFI) (de Graauw et al. 2010), the Photodetector Array Camera and Spectrometer (PACS) (Poglitsch et al. 2010), and the Spectral and Photometric Imaging Receiver (SPIRE) (Griffin et al. 2010). Both PACS and SPIRE consist of bolometer arrays, which are optimal for far-IR to sub-millimeter observations when cooled to very low temperatures, as they are more sensitive in this wavelength range. The telescope itself was of a classic Cassegrain reflector design, having a primary diameter of 3.5 meters, the largest ever for a space-based telescope (Pilbratt et al. 2010). On April 29th, 2013, the last of the liquid helium ran out, and observations ended.



Figure 7: The Herschel Space Observatory. Herschel is a 'cornerstone' ESA mission, with participation from NASA. Image credit: ESA / AOES Medialab.

Photodetector Array Camera and Spectrometer (PACS)

The Photodetector Array Camera and Spectrometer (PACS) (Poglitsch et al. 2010) offers wavelength coverage from 55-210 μm , with 70, 100, and 160 μm filter bands. The detector array covers a field of view of 1.75' by 3.5' using a 64 by 32 pixel bolometer array for the 70 and 100 μm observations, and a 32 by 16 pixel array for 160 μm observations. This provides a pixel scales of approximately 1.2 to 2.4 arcseconds per pixel for the blue/green (70, 100 μm) and red (160 μm) filters, respectively.

Spectral and Photometric Imaging Receiver (SPIRE)

The Spectral and Photometric Imaging Receiver (SPIRE) (Griffin et al. 2010) offers broadband photometry in the 250, 350, and 500 μm filter bands. The instrument covers a field of view of $4'$ by $8'$, utilizing bolometer arrays of 139, 88, and 43 detectors, with pixel scales of 6, 8.3, and 10.8 arc seconds per pixel for the 250, 350, and 500 μm filter bands, respectively. Together, PACS and SPIRE effectively offer coverage from 70–500 μm .

3.4 Surveys

The PACS Evolutionary Probe (PEP) survey, as its name suggests, aimed to provide sufficient data for a more complete understanding of the evolution of star-forming galaxies by utilizing the PACS detector on board *Herschel* (Lutz et al. 2011; Magnelli et al. 2013). This survey, which covered five other so-called “blank” fields in addition to GOODS-S, obtained deep observations totaling approximately 240 hours, reaching 3σ detection sensitivities for the PACS detector (Table 1). In earlier studies, the role of dust had been frequently underestimated due to a number of factors, primarily limitations in resolution. By utilizing *Herschel*'s infrared capabilities, the PEP survey aimed to extend beyond the wavelength range of available data from other space-based telescopes such as *Spitzer*, by providing imaging data for the 70, 100, and 160 μm wave bands. The data were reduced using a standard pipeline for PACS data, in addition to survey-specific procedures (Wieprecht et al. 2009). The reduced and processed data were released in the form of standard Flexible Image Transport System (FITS) image maps, consisting of separate science, error, and coverage maps.

The HerMES survey also aimed to study the evolution of galaxies through observations of star-forming, high redshift galaxies. HerMES, which was the largest project on *Herschel*, is presented in Oliver et al. (2012); Levenson et al. (2010); Viero et al. (2013). Goals for this

survey focused primarily on the infrared study galaxies at redshifts up to $z \sim 3$, covering a large number of fields to an unprecedented depth at these wavelengths (Oliver et al. 2012; Levenson et al. 2010; Viero et al. 2013). For coverage of the GOODS-S field, HerMES provided approximately 20 hours worth of observations, reaching 5σ detection sensitivities as listed in Table 1 via the SPIRE instrument, simultaneously covering the 250, 350, and 500 μm wave bands. Image maps, including flux, noise, and coverage maps, were processed using a standard HIPE (Herschel Interactive Processing Environment) pipeline for SPIRE data (Smith et al. 2012). By combining observations from these two surveys, PEP and HerMES, full coverage was obtained for the infrared emission peak expected for our ILLBGs.

| Survey | Wavelength Coverage | Detection Sensitivities | Pixel Scale | Beam Size (FWHM) |
|-------------------|---------------------|-------------------------|----------------------------------|------------------|
| | μm | mJy | arcsec/pixel ($''/\text{pix}$) | arcsec ($''$) |
| PEP (PACS) | 70 | 0.9 | 1.2 | 5.2 |
| | 100 | 0.6 | 1.2 | 7.7 |
| | 160 | 1.3 | 2.4 | 12 |
| HerMES (SPIRE) | 250 | 8.0 | 6.0 | 18 |
| | 350 | 6.6 | 8.3 | 24 |
| | 500 | 9.6 | 10.8 | 36 |

Table 1: Survey coverage, instrumentation, and detector properties

3.5 Herschel Interactive Processing Environment (HIPE)

The Herschel Interactive Processing Environment (HIPE)⁴ software package was developed for processing, analyzing, and manipulating Herschel data products. In addition to allowing the user access to the Herschel Science Archive products, it offers the ability to process user-provided data from any number of sources. Written in a combination of Java and Python (Jython), HIPE provides the user with a wide array of tasks encompassing photometry, spectroscopy, and other standard analysis procedures. For this work, the data

⁴http://herschel.esac.esa.int/HIPE_download.shtml

provided by the PEP and HerMES surveys were already reduced, with standard pipelines as described in § 3.4. In our analysis, HIPE was utilized primarily for obtaining flux measurements for our ILLBG sample, using the HIPE-provided version of Source Extractor (SExtractor). SExtractor provides photometric measurements by first measuring and subtracting the background for the whole image, then searching for objects with a certain threshold of neighboring pixels, measuring the shape and positions of these objects and cleaning detections, and finally performing photometry on the object. With the HIPE version of SExtractor, the locations of our objects (determined by 24 μm *Spitzer* priors) were given, and photometry performed for the specified beam size for each image, respectively. A summary of these flux measurements can be found in Table 2.

4 ANALYSIS

4.1 Flux Measurements

The publicly available data provided by the PEP and HerMES surveys for the GOODS-S field were loaded into the Herschel Interactive Processing Environment (HIPE), described in detail in § 3.5. Positions of the sources from the *Spitzer* priors were also loaded into HIPE as an ASCII table, and set as a HIPE variable for the source product list. This source list was used as the input for the HIPE version of SExtractor, which produced the measured flux for each of the objects in each filter band in mJy. Objects with secure detections in at least three of the six filter bands (70–500 μm) were used in our modified black body fitting routine. Fluxes measured from *Spitzer* 24 μm data were also obtained and used in the Multi-wavelength Analysis of Galaxy Physical Properties (MAGPHYS) (da Cunha et al. 2008) fitting procedure (§ 4.3), which provided a comparison to our modified black body fits. In addition, 870 μm data from LABOCA (Weiß et al. 2009) was used to provide upper limits for the far-IR SED. The 870 μm flux measurements obtained for our objects were generally above the noise limit of ~ 1.2 mJy/beam (Wieprecht et al. 2009), however, we did not have a secure detection for any object in this filter band. Table 2 lists these fluxes, used for further analysis.

After measuring the fluxes for each object in the 6 filter bands (70–500 μm), the images were inspected individually by eye. This was done not only to check for any flux contamination from nearby objects, but also to verify a secure detection for a given object. As the wavelength increases, the beam area increases, but the resolution of the images decreases (see Figures 8 and 9). For a few of our objects, the measured fluxes are overestimated due

to additional flux from nearby sources in the beam area. Deconvolution techniques may be used to separate these sources; however, these overestimated fluxes were simply not used in fitting our modified blackbody curves.

| Object ID | z | S_{ν} mJy | σ_{ν} mJy | |
|-----------|-------|------------------|-----------------------------|------|
| 1 | 9180 | 1.195 | S_{24} 0.07 [†] | 0.01 |
| | | | S_{70} 0.50* | 0.25 |
| | | | S_{100} 0.70* | 0.19 |
| | | | S_{160} 0.68 | 0.31 |
| | | | S_{250} 6.31 | 1.80 |
| | | | S_{350} 4.32 | 1.70 |
| | | | S_{500} 4.70 | 2.03 |
| | | | S_{870} 1.97 [†] | 0.92 |
| 2 | 9818 | 1.210 | S_{24} 0.14 [†] | 0.01 |
| | | | S_{70} 1.31 | 0.25 |
| | | | S_{100} 2.44 | 0.21 |
| | | | S_{160} 1.26 | 0.34 |
| | | | S_{250} 6.06* | 1.75 |
| | | | S_{350} 1.72* | 1.70 |
| | | | S_{500} 2.53* | 2.04 |
| | | | S_{870} 0 [†] | 0.96 |
| 3 | 10186 | 1.165 | S_{24} 0.14 [†] | 0.01 |
| | | | S_{70} 0.10* | 0.27 |
| | | | S_{100} 0.41 | 0.21 |
| | | | S_{160} 0* | 0.45 |
| | | | S_{250} 13.77 | 1.80 |
| | | | S_{350} 23.40 | 1.70 |
| | | | S_{500} 17.81 | 2.04 |
| | | | S_{870} 2.44 [†] | 0.96 |
| 4 | 10397 | 1.220 | S_{24} 0.06 [†] | 0.01 |
| | | | S_{70} 0.28 | 0.25 |
| | | | S_{100} 0.89 | 0.19 |
| | | | S_{160} 2.14 | 0.32 |
| | | | S_{250} 5.66* | 1.79 |
| | | | S_{350} 1.06* | 1.80 |
| | | | S_{500} 0* | 2.11 |
| | | | S_{870} 0.28 [†] | 0.95 |
| 5 | 11800 | 1.870 | S_{24} 0.08 [†] | 0.01 |
| | | | S_{70} 0.90 | 0.27 |
| | | | S_{100} 2.63 | 0.23 |
| | | | S_{160} 5.67 | 0.36 |
| | | | S_{250} 8.69* | 1.78 |
| | | | S_{350} 12.60* | 1.70 |
| | | | S_{500} 6.45* | 2.08 |
| | | | S_{870} 2.26 [†] | 0.93 |

Table 2: Flux measurements in six Herschel filter bands (70–500 μm), one Spitzer band (24 μm), and one LABOCA band (870 μm) for our sample of ILLBGs. Measurements not used in our fitting procedure are denoted with an asterisk. A dagger denotes the measurement was used in MAGPHYS (§ 4.3), but not included in the modified blackbody curve.

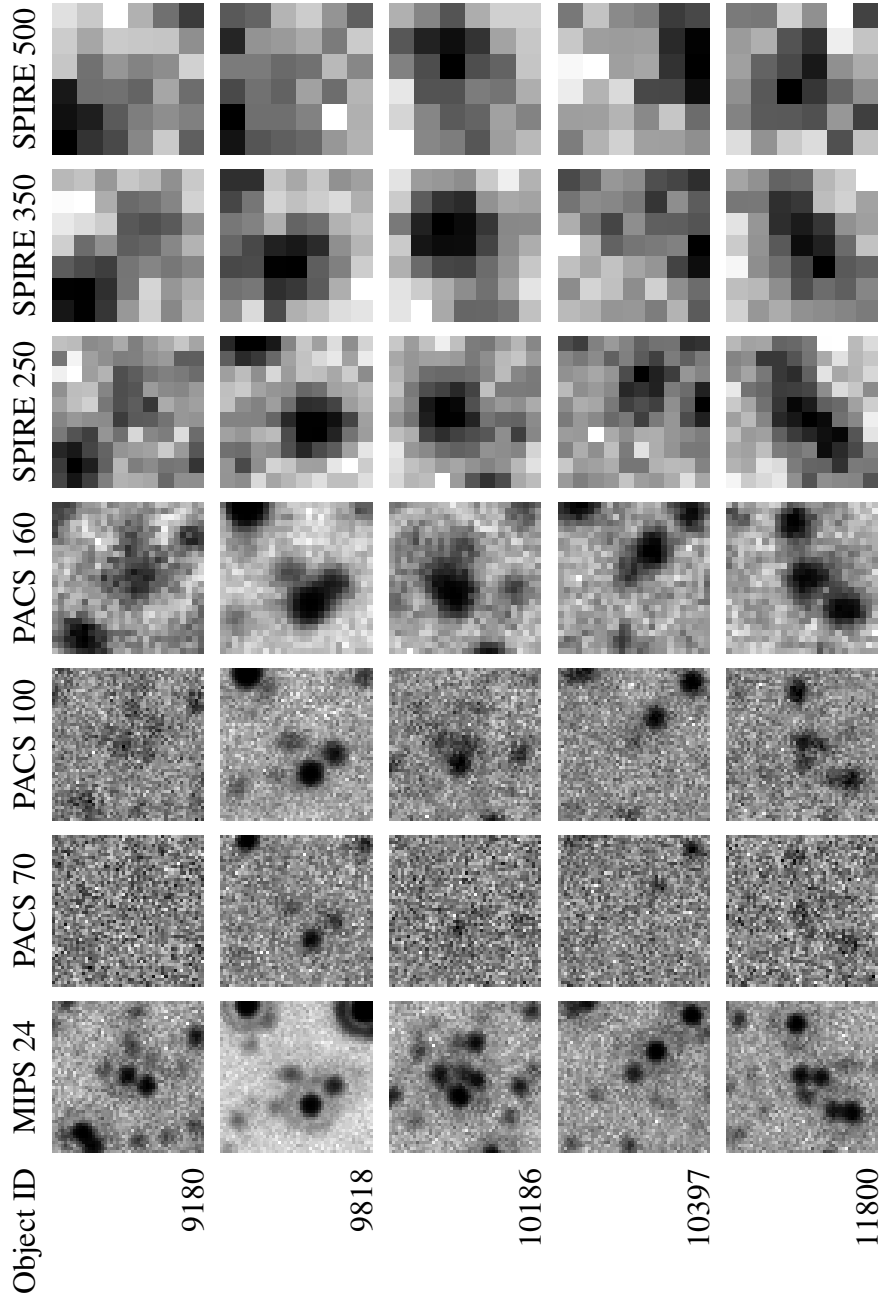


Figure 8: Postage stamp images of our objects with secure detections in at least three of the six filter bands (70–500 μm), with Spitzer 24 μm priors for comparison. The object is located in the center of each image.

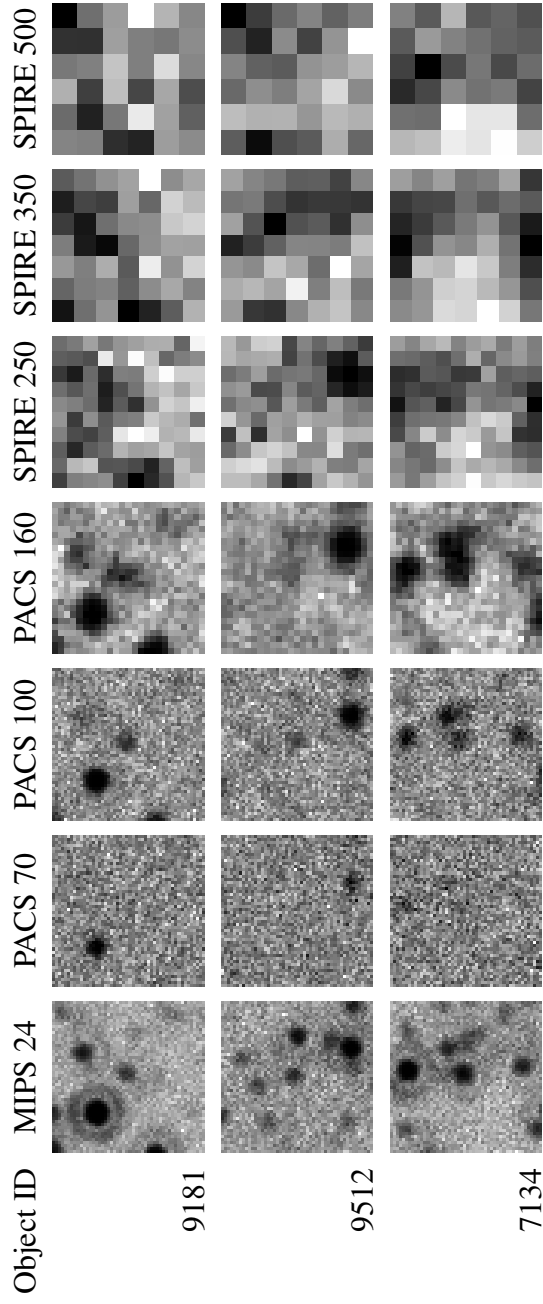


Figure 9: Postage stamp images of those objects which were detected in only two of the six filter bands (70–500 μm), with Spitzer 24 μm priors for comparison. The object is located in the center of each image.

4.2 SED Fitting: Planck Curves

As described in § 2.4, the thermal emission due to dust in our galaxy sample can be modeled as a modified blackbody, or Planck curve. By fitting a modified Planck curve to our far-IR SEDs where we have secure detections (see Table 2), dust temperatures are determined. From our original sample of 14 ILLBGs, 5 galaxies had secure detections in at least three of the six filter bands (70–500 μm). Three galaxies were found to have detections in two of the six filter bands, but were not fitted with a model. Equation 1 describes the curve fit to our data, which depends on the given frequency (ν) (Hilton et al. 2012):

$$S_\nu = A\nu^\beta B(\nu, T_{dust}) \quad (1)$$

where S_ν is the observed flux density, A is the amplitude, β is the emissivity index, and $B(\nu, T_{dust})$ is given as:

$$B(\nu, T) = \frac{2h\nu^3}{c^2} \frac{1}{e^{\frac{h\nu}{k_B T}} - 1} \quad (2)$$

For fitting, we kept the value of β at a fixed value of 1.5, following the procedure outlined in Hilton et al. (2012). This fitting procedure was performed using the IDL program *mpfitfun* (Markwardt 2009), which utilizes a Levenberg-Marquardt least-squares fit when fitting the user-provided function (Equation 1) to a user-provided data set (our flux measurements). With our fitting procedure, we allow two independent variables: the amplitude (A) and the temperature (T_{dust}). From the temperature determined by this fit for each object, the mass of the dust can then be estimated using the equation (Rigopoulou et al. 2010):

$$M_{dust} = \frac{S_{250} D_L^2}{\kappa_{250} B(\nu, T_{dust})} \quad (3)$$

where S_{250} is the flux in the 250 μm filter band, D_L is the luminosity distance, and κ_{250} is the dust mass absorption coefficient. For our fitting, we assume a value of 0.89 $\text{m}^2 \text{kg}^{-1}$ for

κ_{250} as in Hilton et al. (2012), Dunne et al. (2011). The results of our fitting procedure can be found in Figure 10.

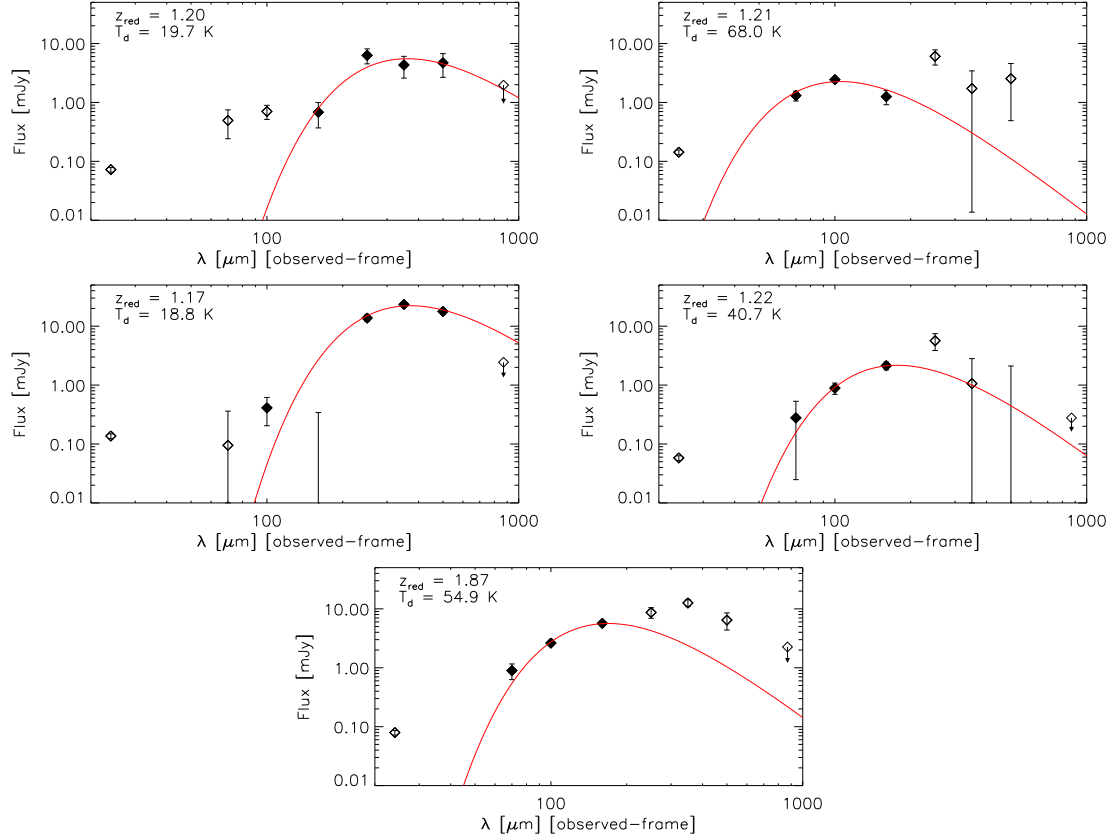


Figure 10: Results from fitting a modified blackbody curve (shown in red) to the far-IR SEDs of our sample of galaxies. Filled diamonds represent flux measurements included in the fit, open diamonds denote fluxes that were not included in the fit, usually due to flux contamination from a nearby object (see § 4.1). The triangle denotes an upper limit given by the $870 \mu\text{m}$ LABOCA data, which was not used in the fit. In the top left corner, the redshift of the galaxy and temperature obtained from the fit is given. Typical uncertainties in T_d are $\sim 5 - 10\%$.

4.3 SED Fitting: MAGPHYS

In addition to our simple modified blackbody, sophisticated dust model fitting procedures, such as the Multi-wavelength Analysis of Galaxy Physical Properties (MAGPHYS) package, (da Cunha et al. 2008) can be used to more accurately fit our observed SEDs. MAGPHYS compares the fluxes provided by the user with a library of model SEDs, and finds the best fit from those models using the method described in da Cunha et al. (2008):

$$\chi_j^2 = \sum_i \left(\frac{L_v^i - w_j \times L_{v,j}^i}{\sigma_i} \right)^2 \quad (4)$$

where L_v^i and $L_{v,j}^i$ are the luminosities in the i^{th} band of the mock galaxy and the j^{th} model, respectively, as described in da Cunha et al. (2008), and w_j is the model scaling factor:

$$w_j = \left(\sum_i \frac{L_v^i L_{v,j}^i}{\sigma_i^2} \right) \left[\sum_i \left(\frac{L_{v,j}^i}{\sigma_i} \right)^2 \right]^{-1} \quad (5)$$

which minimizes the χ^2 value, finding the best model fit for a given SED. From this fit, physical parameters of the galaxy can be calculated. Unlike a modified blackbody fit, MAGPHYS takes into account a number of other factors that may influence the SED for a particular galaxy (see Figure 3). For local ULIRGs, which are comparable to our galaxy sample, Melbourne et al. (2012) shows that the SEDs for these populations of galaxies most likely cannot be fit by a single dust temperature. Therefore, in order to more accurately model the SED for our sample of galaxies, a warm dust component for dust surrounding regions of star formation, as well as a cold dust component for the diffuse ISM must be considered. Compared to the simple modified blackbody fits (Figure 10), MAGPHYS allows for a more robust, realistic interpretation of the SED, accounting for contributions from PAH emission ($\lesssim 15 \mu\text{m}$), the mid-IR continuum ($\lesssim 50 \mu\text{m}$), as well as the thermal emission from both small and large dust grains.

The results of using the MAGPHYS package to fit our data can be found in Figures 11 and 12. For the first set of fits (Figure 11), we fit only those filter bands which were fit with our modified blackbody. As in Figure 10, the flux measurements for filter bands which were not fitted are denoted as open diamonds. While this set of fits offers a reasonable comparison to our modified blackbody fits, we can also fit a wider range of flux measurements (e.g. *Spitzer* 24 μm and LABOCA 870 μm) due to the multiple-component nature of the MAGPHYS package. The results from this set of fits can be found in Figure 12. While the derived parameters do not vary widely from the first set of fits, the dust temperatures produced by these fits are slightly higher on average, which is to be expected, as the 24 μm data helps to better constrain warm dust components.

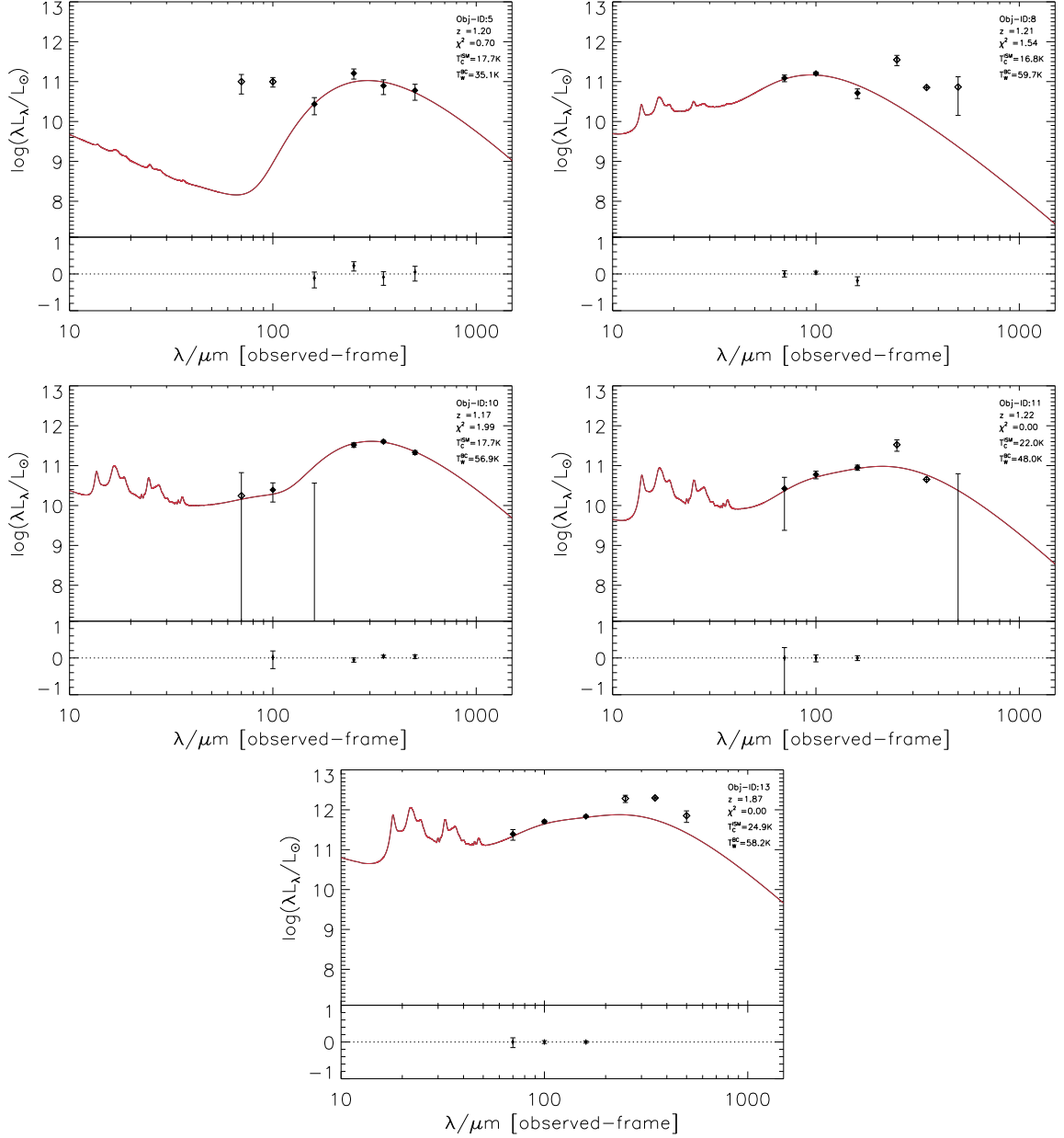


Figure 11: Fit results from MAGPHYS (da Cunha et al. 2012), for those flux measurements included in our modified blackbody fit (see Table 2). As in Figure 10, open diamonds denote flux measurements not used in the fit. The upper right hand corner provides information about each individual object, and the parameters derived from the fit. T_C^{ISM} represents the cold dust component from the ISM, and T_W^{BC} represents the warm dust component from the stellar birth cloud. In the lower section of the plot, residuals $((L_\lambda^{obs} - L_\lambda^{mod}) / L_\lambda^{obs})$ are shown. Typical errors in the temperatures are $\sim 5 - 15\%$.

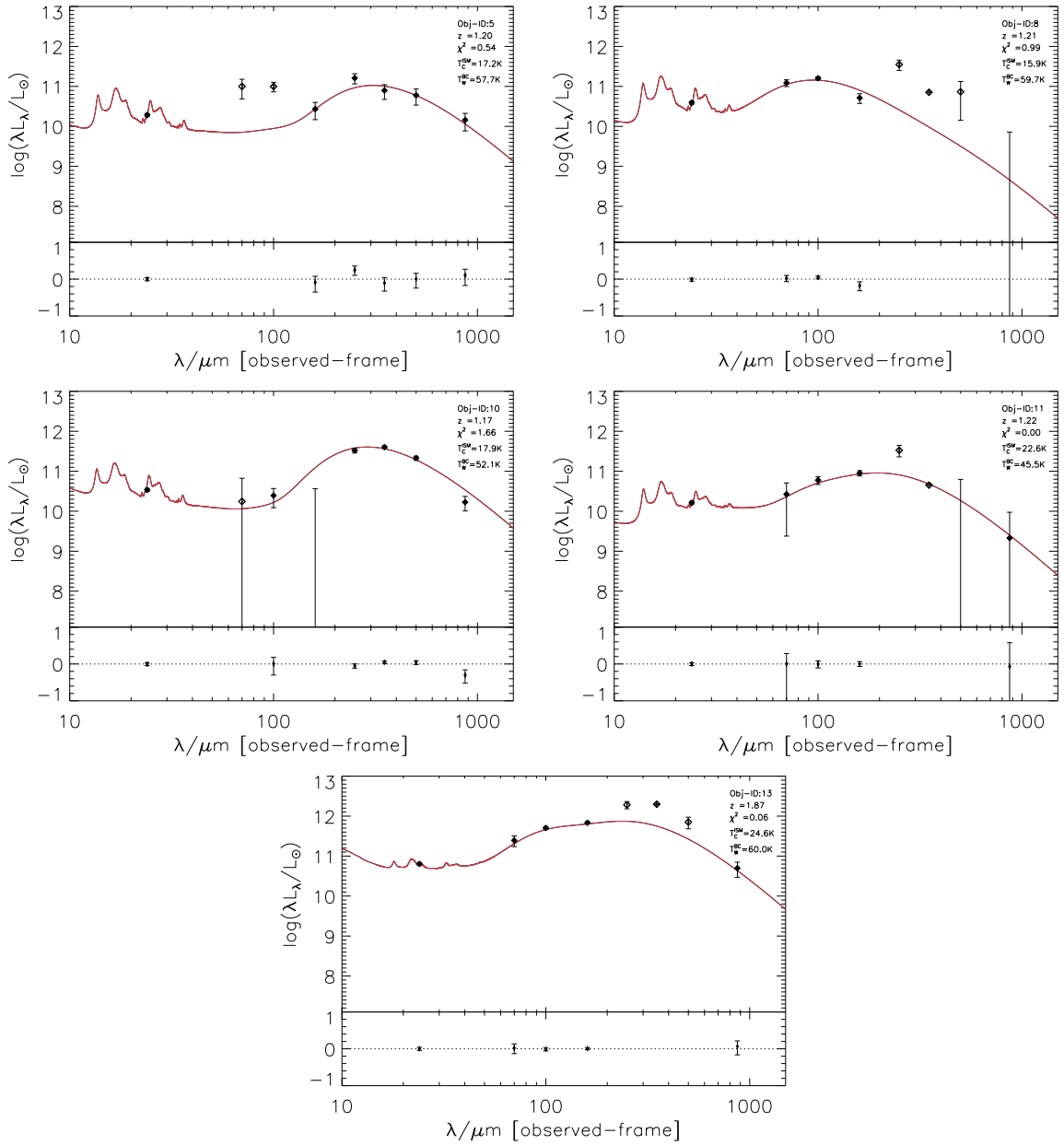


Figure 12: Fit results from MAGPHYS (da Cunha et al. 2012), including the 24 and 870 μm flux measurements. As in Figure 11, open diamonds denote flux measurements not used in the fit. The upper right hand corner provides information about each individual object, and the parameters derived from the fit. T_C^{ISM} represents the cold dust component from the ISM, and T_W^{BC} represents the warm dust component from the stellar birth cloud. In the lower section of the plot, residuals $((L_{\lambda}^{obs} - L_{\lambda}^{mod})/L_{\lambda}^{obs})$ are shown. Typical errors are similar to those in Figure 11.

5 RESULTS AND DISCUSSION

We studied a subsample of 14 ILLBGs from an original sample of 73 LBGs. For five objects in this subsample, we were able to obtain secure detections in at least three of the six PACS/SPIRE filter bands. The far-IR SEDs of these objects were then fitted using two different methods, a modified blackbody (§ 4.2), and MAGPHYS (§ 4.3). From these fits, properties of our ILLBG sample were obtained, such as dust masses, temperatures, and star formation rates. For our modified blackbody fits, we derive temperatures ranging from $\sim 19 - 70$ K. For those objects which have unreasonably low dust temperatures (e.g. objects 1 and 3), we assume an average dust temperature of ~ 45 K, following the approach in Rigopoulou et al. (2010) and Hilton et al. (2012). These dust temperatures are denoted with an asterisk in Table 3. From these temperatures, dust masses are derived, ranging from 5.2×10^6 to $3.3 \times 10^9 M_{\odot}$. For the dust masses derived from our modified blackbody fits (black squares), errors were obtained from *mpfitfun* (Markwardt 2009). Errors for the dust masses derived from our MAGPHYS fits were calculated using the probability distribution functions (PDFs) given for each parameter, and applying the method outlined in Noll et al. (2009):

$$\sigma_x = \sqrt{\frac{\sum_{i=1}^b P_i (x_i - \langle x \rangle)^2}{\sum_{i=1}^b P_i}} \quad (6)$$

where P_i is the PDF for a given parameter, and the weighted expectation value, $\langle x \rangle$ is given by:

$$\langle x \rangle = \frac{\sum_{i=1}^b P_i x_i}{\sum_{i=1}^b P_i} \quad (7)$$

A summary of these results can be found below, in Table 3.

| | Object ID | T_{DP} (K) | T_C (K) | T_W (K) | M_{DP}/M_{\odot} 10^8 | M_{DM}/M_{\odot} 10^8 |
|---|-----------|------------------|----------------|----------------|------------------------------|------------------------------|
| 1 | 9180 | $19.7 \pm 1.5^*$ | 17.2 ± 1.2 | 57.7 ± 9.1 | $0.8 \pm 0.4^*$ | 6.8 ± 2.1 |
| 2 | 9818 | 68.0 | 15.9 ± 3.0 | 59.7 ± 1.6 | 0.1 | 0.1 ± 0.02 |
| 3 | 10186 | $18.8 \pm 0.9^*$ | 17.9 ± 0.8 | 52.1 ± 8.6 | $2.9 \pm 0.7^*$ | 33.0 |
| 4 | 10397 | 40.7 ± 3.5 | 22.6 ± 2.6 | 45.5 ± 7.0 | 0.5 ± 0.3 | 1.3 ± 6.5 |
| 5 | 11800 | 54.9 ± 2.0 | 24.6 ± 2.7 | 60.0 ± 3.0 | 1.5 ± 3.3 | 4.7 ± 2.6 |

Table 3: Galaxy properties obtained from our analysis. T_{DP} denotes the dust temperature obtained through the modified blackbody fit, while T_C and T_W denote the cold and warm dust temperature components derived MAGPHYS (§ 4.3). For those galaxies which had unrealistically low dust temperatures derived from our modified blackbody fit, we assume a dust temperature of ~ 45 K, as in Rigopoulou et al. (2006). These measurements are denoted with an asterisk. M_{DP} denotes the dust mass obtained from the modified blackbody fit, while M_{DM} is the dust mass and estimated via MAGPHYS.

First, we investigate the luminosity correlation for our sample of galaxies (Figure 13). This is simply a measure of the IR luminosity compared to the UV luminosity. UV luminosities were obtained by converting the AB magnitude of our sample of galaxies (see Table 4) into a flux density measurement using the equation (Fukugita et al. 1995):

$$S_{\nu} = 10^{(23.9-AB)/2.5} \quad (8)$$

where the flux density S_{ν} was converted into a flux in W/m^2 , which was then converted into a luminosity using the standard flux-luminosity relation:

$$F = \frac{L}{4\pi D_L^2} \quad (9)$$

where D_L is the luminosity distance. For our sample of galaxies, IR luminosities calculated using the same method as outlined above, using magnitudes from the *Spitzer* 24 μm data. In addition, total IR luminosities were also determined by calculating the total integrated IR flux, using the SED fit by MAGPHYS. This integrated flux was then converted to a luminosity using the same standard relation given above (Equation 9). As our galaxies are

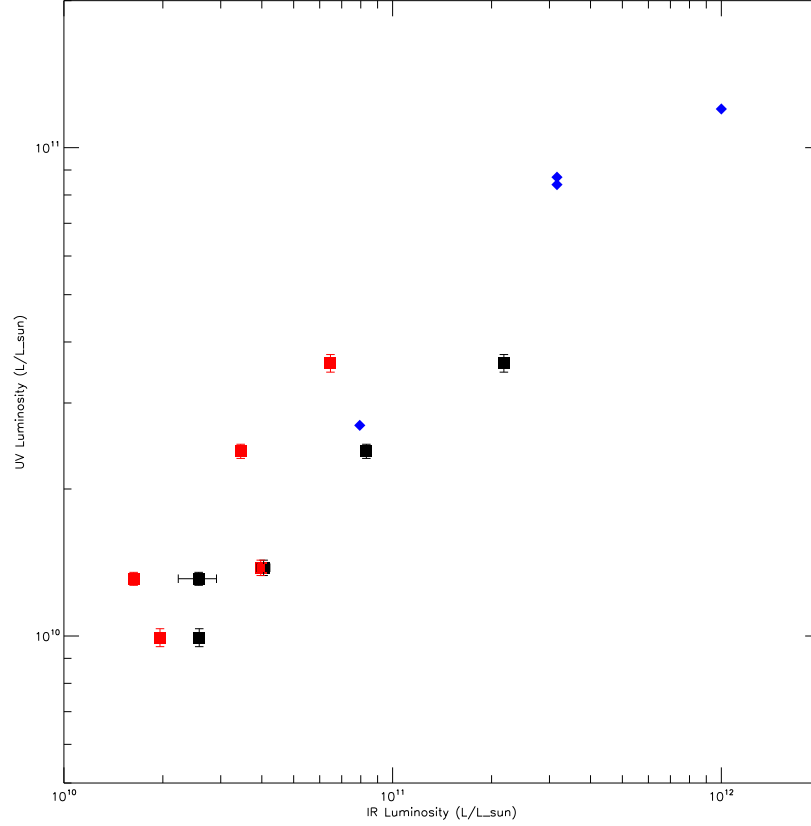


Figure 13: Luminosity correlation for our sample of galaxies and comparable samples. The derivations of the UV and IR luminosities are described below. Squares indicate our sample of 5 ILLBGs, where the black squares indicate the correlation between the UV luminosity and the IR luminosity derived from the integrated IR flux, while the red squares denote the correlation between UV luminosity and the IR luminosity derived from 24 μm magnitudes. Blue diamonds denote average measurements for the $z \sim 3$ LBG samples from Davies et al. (2013).

infrared-luminous (ILLBGs), we see that, for our sample of galaxies, the IR luminosity is about a factor of 5 times higher than the UV luminosity. To examine the validity of this correlation, we compare it with $z \sim 3$ galaxy populations as provided in Davies et al. (2013), which offers a similar sample of infrared-luminous galaxies. From Figure 13, we see that the IR/UV luminosity correlation follows a similar pattern to our $z \sim 2$ ILLBG sample. This correlation indicates that IR flux due to absorption and re-emission by dust contributes a significant portion of the total flux for galaxies in our sample. In addition to showing that our galaxies are indeed infrared-luminous, it provides further evidence that star formation rates may be underestimated if only UV flux is considered.

| Object ID | L_{UV}/L_{\odot} 10^{10} | L_{IR}/L_{\odot} 10^{10} | L_{24}/L_{\odot} 10^{10} | SFR_{UV} [M_{\odot}/year] | SFR_{IR} [M_{\odot}/year] |
|-----------|---------------------------------|---------------------------------|---------------------------------|---|---|
| 1 9180 | 1.0 ± 0.1 | 2.6 ± 0.1 | 2.0 ± 0.01 | 2.5 ± 0.1 | 4.5 ± 1.2 |
| 2 9818 | 1.4 ± 0.1 | 3.5 ± 0.2 | 4.0 ± 0.01 | 3.4 ± 0.1 | 7.0 ± 0.9 |
| 3 10186 | 2.4 ± 0.1 | 7.8 ± 0.3 | 3.5 ± 0.01 | 6.0 ± 0.2 | 14.4 ± 0.9 |
| 4 10397 | 1.3 ± 0.1 | 2.7 ± 0.3 | 1.6 ± 0.01 | 3.3 ± 0.1 | 4.5 ± 0.3 |
| 5 11800 | 3.6 ± 0.2 | 240 ± 20.0 | 6.5 ± 0.01 | 9.1 ± 0.2 | 37.7 ± 4.2 |

Table 4: UV and IR luminosities used in Figure 13, as well as the star formation rates as derived below, and used in Figure 14.

An important comparison to draw from these results is between the stellar mass, and the calculated star formation rate. As explained in § 2.3, the amount of star formation in our sample of galaxies may be underestimated due to absorption by dust, which re-emits the UV photons from young, bright stars as thermal emission. We see this result clearly in Figure 13, therefore, in order to properly calculate the rate of star formation within our galaxies, we have to take into account this absorption process. Figure 14 illustrates the effect of this underestimation. The SFR estimate derived from the UV luminosity (Figure 14, black squares) is consistently lower than the SFR derived from IR flux measurements (Figure 14, red squares). Star formation rates are derived using the following relation (Madau & Dickinson 2014):

$$SFR = \kappa_{FUV} \times L_{\nu}(FUV) \quad (10)$$

with the FUV conversion factor:

$$\kappa_{FUV} = 2.5 \times 10^{-10} M_{\odot} \text{yr}^{-1} L_{\odot}^{-1} \quad (11)$$

The SFR derived from the IR was calculated by the same process as the UV, instead with the IR luminosities, and using the IR conversion factor given in Madau & Dickinson (2014):

$$\kappa_{IR} = 1.73 \times 10^{-10} M_{\odot} \text{yr}^{-1} L_{\odot}^{-1} \quad (12)$$

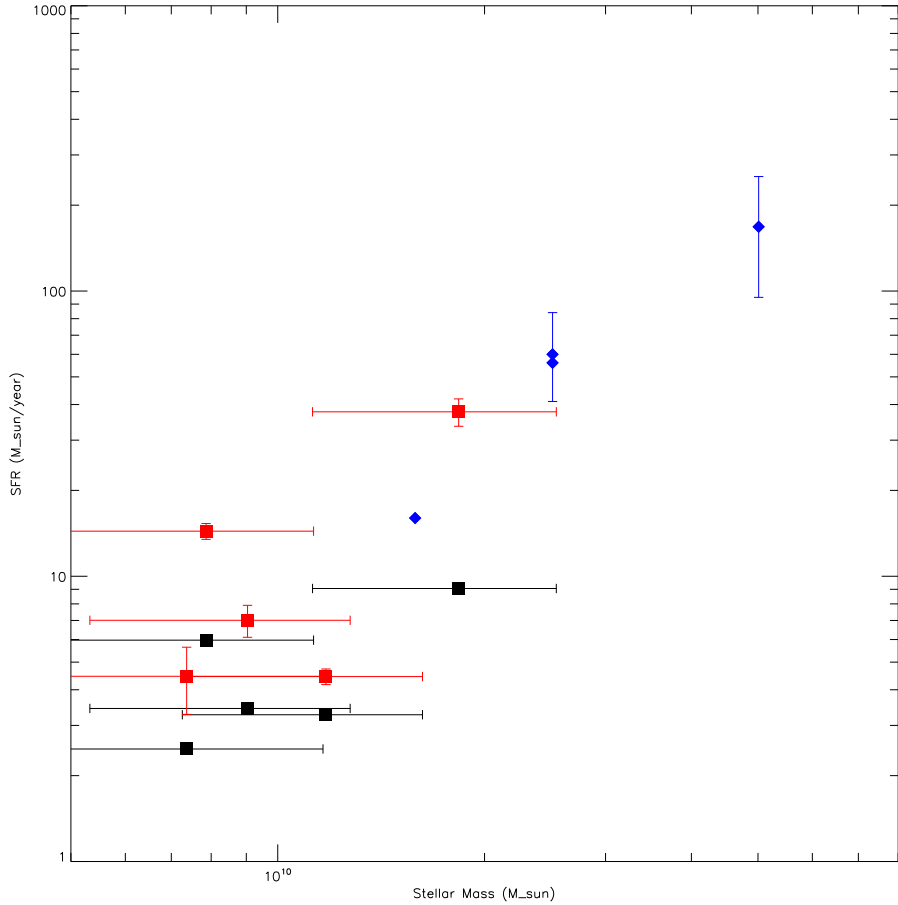


Figure 14: Stellar mass vs star formation rate. Here, squares indicate our subsample of 5 ILLBGs, where black squares denote the SFR calculated using the UV luminosity of the galaxy, and the red squares indicate the SFR calculated using the IR luminosity. Blue diamonds denote average values for the $z \sim 3$ LBG samples given by Davies et al. (2013).

As in Figure 13, we use average values for $z \sim 3$ galaxy populations described in Davies et al. (2013) as a comparison to our sample. We see that on average, the overall SFR rates compare well to the $z \sim 3$ galaxies, although in both cases, the SFRs for our sample of galaxies are lower. While this is the opposite of what we would expect for the global star

formation rate (see Figure 1), we keep in mind that our sample is small, while the values given by Davies et al. (2013) are averages over a whole population of galaxies. In this sense, it is reasonable that the SFRs for our small sample are comparable, although not representative, of the ILLBG population at $z \sim 2$.

Another interesting comparison we can examine is the ratio of dust mass to stellar mass in our galaxy sample (Figure 15). By comparing trends in the dust/stellar mass ratio of our galaxy sample to other populations of galaxies, we can examine the role of dust in galaxy evolution. As shown in Figure 15, the ratio of dust mass to stellar mass in our sample of ILLBGs is higher relative to other galaxy populations, such as the KINGFISH survey (Kennicutt et al. 2011), the *Herschel* Virgo Cluster Survey (Davies et al. 2010), and submillimeter galaxies (SMGs) (Michałowski et al. 2010). This is somewhat to be expected, as the dust plays a crucial factor in the detection of these ILLBGs. If a significant amount of dust did not exist in these galaxies, a larger portion of their UV flux would escape, and would not be absorbed and remitted in the IR. In addition, our galaxies may have a higher dust to stellar mass ratio due to that fact that our ILLBG sample was selected due to significant far-IR luminosities. In this sense, our galaxy sample is most comparable to SMGs at $z \sim 3$, as they are typically selected for being IR luminous (Michałowski et al. 2010). As stated in § 4.1, a number of our objects were not fitted at certain wavelengths due to flux contamination by nearby objects. For those wavelengths that were fitted, there is still the possibility that there exists some additional flux from neighboring objects due to the widening of the beam size and lower spatial resolution at longer wavelengths.

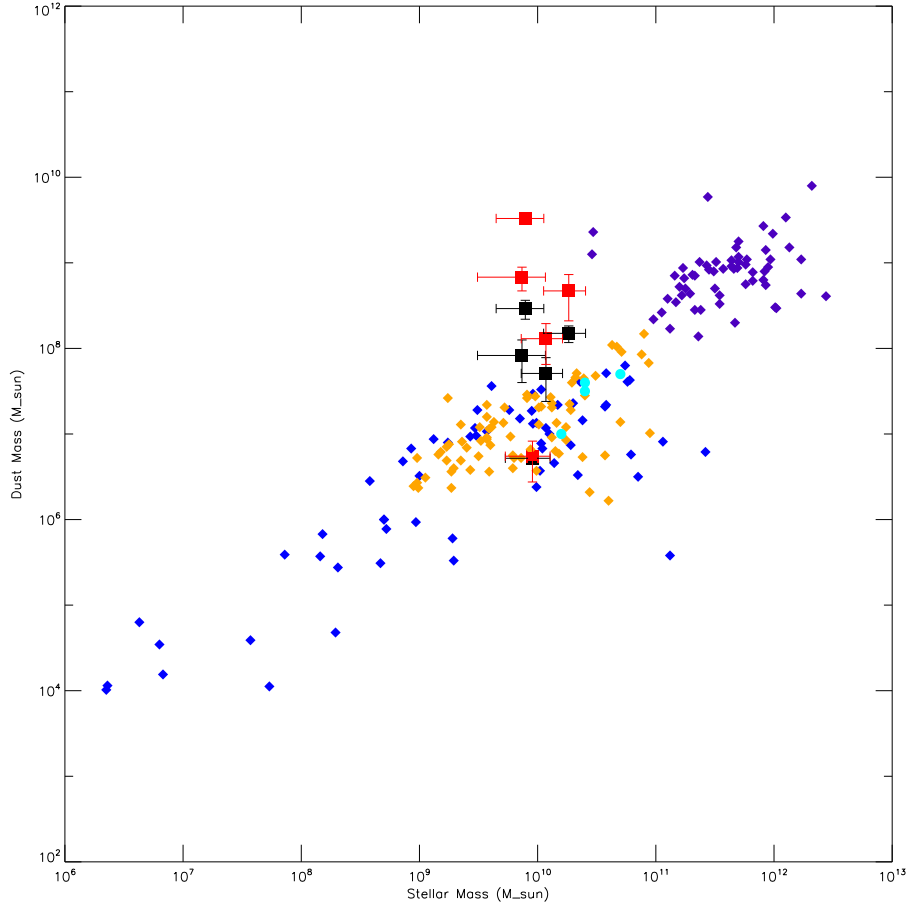


Figure 15: Comparison of our galaxy sample with other galaxy populations. Our sample of 5 ILLBGs is denoted by the square symbols, where the black squares denote the dust mass determined from our simple modified blackbody fit, and the red squares denote the dust mass determined using the MAGPHYS package. Blue diamonds represent mass estimates from the HerschelKINGFISH (Key Insights on Nearby Galaxies: A Far-Infrared Survey with Herschel) survey (Kennicutt et al. 2011), which explored a sample of 61 nearby galaxies. Orange diamonds denote results from the Herschel Virgo Cluster Survey (Davies et al. 2010), which provides a representative sample of 78 optically bright Virgo Cluster galaxies. Purple diamonds represents a sample of sub-mm galaxies (Michałowski et al. 2010) at redshifts $5 \leq z \leq 6.5$.

6 SUMMARY AND CONCLUSIONS

In this work, we have studied a subsample of 14 ILLBGs from an original sample of 73 LBGs, finding 5 objects with secure detections in at least three of the six filter bands (70–500 μm). Three additional objects were found to have detections in two of the six filter bands, but were not used in further analysis. These objects were color-magnitude selected as described in Habertzettl et al. (2012) for their high IR luminosities (ILLBGs). By measuring the fluxes of these objects, we were able to fit the far-IR SED of these objects with a simple modified blackbody curve as described in Hilton et al. (2012). For two of the five objects, unrealistically low dust temperatures were determined, and an average dust temperature of ~ 45 K was assumed, from Rigopoulou et al. (2006). While these simple modified blackbody fits give good estimations, our dust SEDs were also fit using a more complex model via the MAGPHYS package (da Cunha et al. 2012). MAGPHYS offers a more realistic approach to fitting our dust SEDs, as it takes into account both warm and cold dust components. Two MAGPHYS fits were obtained: one using only those flux measurements that were fit with the modified blackbody curve, and one that utilized a wider range flux measurements (e.g. 24 and 870 μm). We find that while the results are not drastically different, taking these additional flux measurements into account does affect the shape of the fit, and therefore the parameters derived from the fit. These parameters, such as dust masses and temperatures for each method were then compared to other star-forming galaxy populations. Our conclusions are as follows:

- Derived UV and IR luminosities for our objects follow a similar trend to averages of $z \sim 3$ galaxy populations as described in Davies et al. (2013). When we compare the IR luminosities derived from $24 \mu\text{m}$ to those derived from the integrated IR flux ($8\text{--}1000 \mu\text{m}$), we find that the former is lower by a factor of ~ 2 . This is somewhat expected, as the integrated flux includes contributions over the whole wavelength range, which for our objects peaks between $100\text{--}1000 \mu\text{m}$.
- On average, our SFR estimates are moderate compared to those in Davies et al. (2013), and are underestimated by a factor of ~ 5 when derived from UV luminosities as compared to the SFR derived from the IR luminosities. Hilton et al. (2012) finds the SFR derived from IR combined with the SFR derived from the UV is a factor of 2 higher than the SFR derived from UV alone, which is consistent with our findings. As our LBGs are selected to be infrared-luminous (ILLBGs), dust in these galaxies is expected to obscure a significant amount of UV flux from young, bright stars. From this result, we see that this effect due to dust must be considered to accurately determine star formation rates for our sample of galaxies.
- When we compare the ratio of our dust mass to stellar mass for our galaxy sample to other star forming galaxy populations at various redshifts, we find that the dust mass ratio is higher for our sample of galaxies. This may be due to the selection criteria used, as our subsample specifically contains those galaxies which are infrared-luminous, and therefore expected to have a larger percentage of dust. From Figure 15, we see that our galaxy sample is comparable to the SMG sample given by Michałowski et al. (2010).

Overall, the analysis of the dust properties for our subsample of ILLBGs provides a reasonable comparison to other populations of star-forming galaxies at various redshifts. Although our sample size is small, we find that our objects compare reasonably well to galaxy

populations at $z \sim 3$ (Davies et al. 2013), as well as populations of SMGs at higher redshifts (Michałowski et al. 2010). Higher resolution data (such as observations from ALMA) could be used to obtain a more complete set of flux measurements, giving better measurements that are currently constrained by low-resolution 870 μm LABOCA data, which may aid in further constraining the model SEDs for our sample of galaxies, and therefore their derived parameters. In addition, a larger sample of ILLBGs (e.g. from another “blank” field, such as GOODS-N), could be used to more accurately characterize ILLBGs at $z \sim 2$. With a better understanding of these parameters which affect the galaxy evolution, such as dust masses and SFRs, we can more correctly describe the role of dust in star formation, and therefore evolutionary processes in galaxy populations at this redshift.

REFERENCES

- Adelberger, K. L., Steidel, C. C., Shapley, A. E., et al. 2004, *ApJ*, 607, 226
- Baldry, I. K. 2008, *ag*, 49, 050000
- Bolzonella, M., Miralles, J.-M., & Pelló, R. 2000, 363, 476
- da Cunha, E., Charlot, S., Dunne, L., Smith, D., & Rowlands, K. 2012, in *IAU Symposium*, Vol. 284, IAU Symposium, ed. R. J. Tuffs & C. C. Popescu, 292–296
- da Cunha, E., Charlot, S., & Elbaz, D. 2008, 388, 1595
- Daddi, E., Cimatti, A., Renzini, A., et al. 2004, *ApJ*, 617, 746
- Dale, D. A., Helou, G., Contursi, A., Silbermann, N. A., & Kolhatkar, S. 2001, *ApJ*, 549, 215
- Davies, J. I., Baes, M., Bendo, G. J., et al. 2010, 518, L48
- Davies, L. J. M., Bremer, M. N., Stanway, E. R., & Lehnert, M. D. 2013, 433, 2588
- de Graauw, T., Helmich, F. P., Phillips, T. G., et al. 2010, 518, L6
- Dunne, L., Gomez, H. L., da Cunha, E., et al. 2011, 417, 1510
- Eggen, O. J., Lynden-Bell, D., & Sandage, A. R. 1962, *ApJ*, 136, 748
- Elbaz, D., Dickinson, M., Hwang, H. S., et al. 2011, 533, A119
- Fukugita, M., Shimasaku, K., & Ichikawa, T. 1995, *PASP*, 107, 945
- Griffin, M. J., Abergel, A., Abreu, A., et al. 2010, 518, L3
- Haberzettl, L., Williger, G., Lehnert, M. D., Nesvadba, N., & Davies, L. 2012, *ApJ*, 745, 96
- Hilton, M., Conselice, C. J., Roseboom, I. G., et al. 2012, 425, 540
- Hirashita, H. & Ferrara, A. 2002, 337, 921
- Hubble, E. P. 1927, *The Observatory*, 50, 276
- Kennicutt, R. C., Calzetti, D., Aniano, G., et al. 2011, *PASP*, 123, 1347
- Levenson, L., Marsden, G., Zemcov, M., et al. 2010, 409, 83

Lutz, D., Poglitsch, A., Altieri, B., et al. 2011, 532, A90

Madau, P. & Dickinson, M. 2014, *astroph*

Magdis, G. E., Rigopoulou, D., Huang, J.-S., & Fazio, G. G. 2010, 401, 1521

Magnelli, B., Popesso, P., Berta, S., et al. 2013, 553, A132

Markwardt, C. B. 2009, in *Astronomical Society of the Pacific Conference Series*, Vol. 411, *Astronomical Data Analysis Software and Systems XVIII*, ed. D. A. Bohlender, D. Durand, & P. Dowler, 251

Melbourne, J., Soifer, B. T., Desai, V., et al. 2012, 143, 125

Michałowski, M., Hjorth, J., & Watson, D. 2010, 514, A67

Noll, S., Burgarella, D., Giovannoli, E., et al. 2009, 507, 1793

Oliver, S. J., Bock, J., Altieri, B., et al. 2012, 424, 1614

Petty, S. M., de Mello, D. F., Gallagher, III, J. S., et al. 2009, 138, 362

Pilbratt, G. L., Riedinger, J. R., Passvogel, T., et al. 2010, 518, L1

Poglitsch, A., Waelkens, C., Geis, N., et al. 2010, 518, L2

Reddy, N. A., Steidel, C. C., Pettini, M., et al. 2008, 175, 48

Rigopoulou, D., Huang, J.-S., Papovich, C., et al. 2006, *ApJ*, 648, 81

Rigopoulou, D., Magdis, G., Ivison, R. J., et al. 2010, 409, L7

Shapley, A. E., Steidel, C. C., Adelberger, K. L., et al. 2001, *ApJ*, 562, 95

Smith, A. J., Wang, L., Oliver, S. J., et al. 2012, 419, 377

Steidel, C. C. & Hamilton, D. 1992, 104, 941

Steidel, C. C., Shapley, A. E., Pettini, M., et al. 2004, *ApJ*, 604, 534

Steinmetz, M. & Navarro, J. F. 2002, 7, 155

Takeuchi, T. T. & Ishii, T. T. 2004, 426, 425

Toomre, A. & Toomre, J. 1972, *ApJ*, 178, 623

Viero, M. P., Wang, L., Zemcov, M., et al. 2013, *ApJ*, 772, 77

Webb, T. M., Eales, S., Foucaud, S., et al. 2003, *ApJ*, 582, 6

Weiß, A., Kovács, A., Coppin, K., et al. 2009, *ApJ*, 707, 1201

Wieprecht, E., Schreiber, J., de Jong, J., et al. 2009, in *Astronomical Society of the Pacific Conference Series*, Vol. 411, *Astronomical Data Analysis Software and Systems XVIII*, ed. D. A. Bohlender, D. Durand, & P. Dowler, 531

CURRICULUM VITAE

Jennifer L. Wojno
602 Ruggles Place, Apt. 324
Louisville, KY 40208
(859) 248-6863
j0wojn01@louisville.edu

Education

University of Louisville, Louisville, KY
Master's Program, Physics
August 2012 - Present

University of Louisville, Louisville, KY
B.S. in Physics, focus in Astronomy and Astrophysics
2009 - 2012, awarded in May 2012

Carol Martin Gatton Academy for Mathematics and Science in Kentucky
Western Kentucky University, Bowling Green, KY
2007 - 2009

Scholarships and Awards

University of Louisville, Hallmark Trustee's Scholarship, 2009 - 2012

Research Experience

Internship, University of Arkansas, Fayetteville, AR
May 2011 - July 2011

Participated in the Research Experience for Undergraduates Program, funded by the National Science Foundation. Assisted Dr. Claud Lacy with research on stellar evolution using binary star system TY Tau, processing data using a series of specialized programs. Utilized photometric and spectroscopic data to characterize the system.

Internship, University of Nevada, Las Vegas, Las Vegas, NV
June 2010 - August 2010

Participated in the Research Experience for Undergraduates Program, funded by the National Science Foundation. Conducted high pressure physics research under Dr. Michael Pravica and graduate assistant Martin Galley, assisting in data acquisition and analysis of various secondary explosives. Focused primarily on infrared spectroscopy and analysis.

Publications and Conference Presentations

223rd Meeting of the American Astronomical Society, January 2014

Presented a poster titled *Herschel-detected LBGs at $z \sim 2$* . 2014AAS...22324660W

222nd Meeting of the American Astronomical Society, June 2013

Presented a poster titled *Dust Properties of Star Forming Galaxies at $z \sim 2$* .

220th Meeting of the American Astronomical Society, June 2012

Presented a poster titled *Photometric and Spectroscopic Analysis of Eclipsing Binary TY Tau*. 2012AAS...22052312W

A High Pressure, High Temperature Study of 1,1 Diamino-2,2 Dinitro ethylene.
Michael Pravica, Martin Galley, Changyong Park, Harrison Ruiz and Jennifer Wojno
2011, High Press. Res., 31:80-85

Teaching

Graduate Teaching Assistant, University of Louisville, August 2012 - present

Teaching assistant for multiple sections of an entry-level astronomy lab (PHYS 108). Organize weekly lab meetings and activities, assist students when necessary, grade assignments completed by students.

Undergraduate Teaching Assistant, University of Louisville, January 2012 - May 2012

Teaching assistant for entry-level physics lab (PHYS 223). Provided students with support and guidance where necessary, graded weekly lab reports submitted by students.

Professional Societies

Junior Member, American Astronomical Society

Member, Society of Physics Students (local and national)

Member, Sigma Pi Sigma

Skills

Astronomical Skills

Herschel Interactive Processing Environment (HIPE)

SExtractor

Basic knowledge of IDL, IRAF

Miscellaneous Skills

Unix/Linux operating systems

Microsoft Windows operating systems

C, C++, Perl

Wolfram Mathematica